Available online at www.sciencedirect.com
SCIENCE DIRECT®
International Journal of Heat and Mass Transfer 49 (2006) 3298–3312
International Journal of HEAT and MASS TRANSFER
www.elsevier.com/locate/ijhmt

Flow bifurcation due to opposing buoyancy in two vertically connected open cavities

Yuguo Li [a,*], Pengcheng Xu [a,b], Hua Qian [a], Qi-Hong Deng [a,c], Jingyi Wu [d]

[a] Department of Mechanical Engineering, The University of Hong Kong, Pokfulam Road, Hong Kong SAR, China
[b] Institute of Applied Mathematics, Academy of Mathematics and Systems Sciences, Chinese Academy of Sciences, Beijing, China
[c] School of Energy and Power Engineering, Central South University, Changsha, Hunan, China
[d] School of Mechanical and Power Engineering, Shanghai Jiao Tong University, Shanghai, China

Received 14 February 2005; received in revised form 13 December 2005
Available online 22 May 2006

Abstract

A bifurcation behaviour of flows driven by opposing buoyancy in two vertically connected open cavities was found and investigated using flow visualization experiments, theoretical analysis and computational fluid dynamics simulations. In the theoretical analysis, the fluid in each cavity was assumed to be fully mixed. It was found that two stable fixed points exist for a certain range of strength ratios of the heat source/sink. Hysteresis phenomenon was found between the two stable steady flows. The simple theoretical analysis suggests that two Hopf bifurcations also occur. Both computational fluid dynamics simulations and flow visualization confirm the existence of two stable solutions.
© 2006 Elsevier Ltd. All rights reserved.

Keywords: Buoyancy flows; Hysteresis phenomenon; Hopf bifurcation; Open cavity; Computational fluid dynamics; Non-linear analysis

1. Introduction

Due to their significance in many engineering applications, buoyancy-driven flows (i.e., thermal convection, fluid motion set up by heating and cooling processes) have been extensively studied in various different configurations, such as natural convection in enclosed cavities (e.g., [1]) and open cavities (e.g., [2]) with heated boundaries. It is known that buoyancy-driven flows can exhibit various dynamical phenomena. For example, in the well-known Rayleigh–Bernard convection problem, the cavity has two differentially heated horizontal walls, with a cold top, a hot bottom and two adiabatic side walls. When the Rayleigh number (*Ra*) increases, the flow is shown to undergo transitions from a state of pure conduction to steady cellular flow, periodic flows, quasi-periodic flows, chaotic flows and ultimately turbulent flows (e.g., [3]). Jahnke et al. [4] numerically investigated convection in an enclosed cavity, where the upper half of the side walls was relatively cold while the lower half was relatively warm. As *Ra* increases, the flow undergoes transitions from a two (2) by two (2) steady cellular flow to a pitchfork bifurcation, a Hopf bifurcation leading to oscillatory flows etc.

One interesting class of buoyancy-driven flows involves a nearly direct opposition of two buoyancy forces. The pioneering work of Stommel [5] showed that two different flow regimes existed in two horizontally connected cavities in which the flow was driven by opposing buoyancy forces due to heat and salinity. His work initiated much research effort on the existence of alternative ocean currents and multiple flow states in estuaries, shelves and marginal seas (e.g., [6–10]). A different but related flow configuration was suggested by Keller [11] and Welander [12], i.e., a differentially heated fluid loop subjected to a heat source at the top and a heat sink at the bottom. Periodic oscillations were found in a one-dimensional mode of thermal convection due to opposing buoyancy forces. Subsequent work

* Corresponding author. Tel.: +852 2859 2625; fax: +852 2858 5415.
E-mail address: liyg@hku.hk (Y. Li).

0017-9310/$ - see front matter © 2006 Elsevier Ltd. All rights reserved.
doi:10.1016/j.ijheatmasstransfer.2006.03.016

Nomenclature

A	opening area (m^2)
b	variable used in Eq. (5)
C	specific heat of thermal mass (fluid) (J/kg K)
C_D	discharge coefficient
C_p	specific heat of fluid at constant pressure (J/kg K)
E	heat source (W)
h	height between two openings in each cavity (m)
k	turbulence kinetic energy (W)
M	weight of thermal mass (fluid) (kg)
p	pressure (Pa)
q	flow rate of fluid through opening (m^3/s)
Ra	Rayleigh number
Re	Reynolds number
t	time (s)
T	temperature (K)
u, v	velocity component at x- and y-direction, respectively (m/s)

Greek symbols

β	fluid expansion coefficient
ε	dissipation rate of turbulence kinetic energy (m^2/s^2)
θ	temperature difference (K)
κ	thermal diffusivity (m^2/s)
λ	eigenvalue of a matrix
ν	kinetic viscosity (m^2/s)
ν_t	turbulence kinetic viscosity (m^2/s^3)
ρ	fluid density (kg/m^3)
σ_k	turbulence diffusion coefficients for k
σ_t	turbulent diffusion coefficients for T
σ_ε	turbulence diffusion coefficients for ε
τ	a variable related to time, used in Eq. (5)

Subscripts

b	bottom opening
m	middle opening
t	top opening
1	zone 1 or lower cavity
2	zone 2 or upper cavity
0	ambient

showed that much richer dynamical phenomena such as the Lorenz-like chaotic flow (i.e., aperiodic flow with successive direction alternation) exists. A good review of research on natural circulation loops can be found in the works of Greif [13] and Jiang et al. [14].

None of references on the opposing buoyancy-driven cavity flows cited above considered open cavities. Cavity flow with openings can be found in a wide range of engineering applications, e.g., natural ventilation and passive cooling of buildings, natural venting of smoke flows and fire spread in buildings, cold and hot water storage/circulation, and solar hot water systems. In this paper, we rotate the classical two-cavity ocean model of Stommel [5] by 90° and allow both cavities to directly open to the ambient environment. The two vertically connected cavities both have two openings, with a heat source in the upper cavity and a heat sink in the lower cavity. A simple flow visualization experiment using salt water to model opposing buoyancy forces shows the existence of two stable flow regimes. A simple macroscopic model is then presented in which uniform fluid temperature distribution is assumed in each cavity. The flow resistance through openings is considered by a simple pressure loss coefficient. We derive a simple system of non-linear ordinary differential equations that governs the flow rate through the system and the heat balance in each cavity. Non-linear dynamical system analysis of the governing equations demonstrated the existence of two stable flow regimes, as well as two Hopf bifurcations. The bi-stable convection flows are further studied using computational fluid dynamics with a bi-section continuation algorithm.

2. Experimental

2.1. A simple model of two vertically connected cavities with openings

Two vertically connected cavities with a top opening and a bottom opening are considered (see Fig. 1(a)). The bottom cavity has a heat source of strength E_1 (>0) and the top one has a heat sink of strength E_2 (<0). All

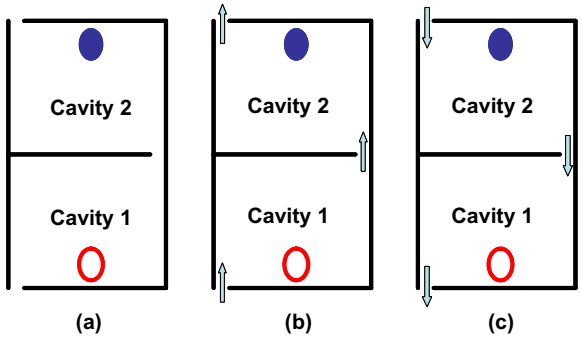

Fig. 1. The geometry and notation of the two vertically connected cavities with a positive buoyancy force in the lower cavity and a negative buoyancy force in the upper cavity (a). Two flow patterns are possible, i.e., an upward flow pattern (b), and a downward flow pattern (c).

boundaries of the two cavities are adiabatic. It is obvious that at least two flow patterns, i.e., an upward flow or a downward flow, are possible depending on the direction of the overall buoyancy force (Fig. 1(b) and (c)). If the overall buoyancy force is positive, the flow is upward; and if the overall buoyancy force is negative, a downward flow is expected. Depending on the heat source strength and size, a thermal plume may be formed in a cavity. A study of thermal plumes in an open cavity showed that the flow might be stratified [15]. We first present flow visualization results to illustrate the existence of two flow regimes using a simple 'fish tank' experimental set-up.

2.2. Experimental set-up

A two-cavity perspex tank was constructed with each cavity having the dimensions of 20 cm (long) × 20 cm (wide) × 10 cm (high) (Fig. 2). A 20 × 1.5 cm opening connected the two cavities. Two openings of the same size were made in the ceiling of the upper cavity and in the floor of the lower cavity. In the two bottom and top walls, there were also 40 small holes, each 1 mm in diameter, for providing a 'heat' source and sink, respectively. The two-cavity tank was placed inside a large water tank (78 × 38 × 54 cm), which simulated a neutral ambient environment. Different concentrations of salt water were used to model the buoyancy forces. The salt water method was used successfully for modeling natural ventilation flow in buildings (e.g., [15,16]).

The positive buoyancy flux in the lower cavity was created by supplying a constant flow rate of fresh water with a density of 997.64 kg/m^3, while the negative buoyancy in the upper cavity was created by supplying a constant flow rate of water with a relatively high concentration of salt (11.45% by weight) with a density of 1068.84 kg/m^3. In the large tank, a medium concentration of salt water (5.725% by weight) with a density of 1033.24 kg/m^3 was used. The density difference between the ambient water of medium salt concentration and the positive 'heat' source was the same as that between the negative 'heat' sink in the upper cavity and the ambient water. With this design, it was relatively easy to achieve the same absolute strength of the two buoyancy forces by providing the same flow rate.

For dynamic similarity, we consider the Reynolds number (Re) and the Rayleigh number (Ra) [17]

$$Re = \frac{(g'H)^{1/2}H}{v}$$

$$Ra = \frac{g'H^3}{\kappa v}$$

where g' is the reduced gravity of the flow ($g\Delta\rho/\rho$), κ is diffusivity of heat in air for full-scale or salt in water, and v is the kinetic viscosity.

We use the subscripts L and F to denote laboratory-scale and full-scale, respectively. For a full-scale flow driven by a temperature difference of 10 °C, $g'_F = 0.33$ m/s^2 at 300 K, with $v_F = 1.6 \times 10^{-5}$ m^2/s, $\kappa = 2.28 \times 10^{-5}$. If $H_F = 3$ m, we have $Re_F = 1.86 \times 10^5$ and $Ra_F = 2.44 \times 10^{10}$. For a small-scale brine-water experiment where $H_L \sim 0.1$ m with the density difference $\Delta\rho = 35.6$ kg/s, $g'_L = 0.356$ m/s^2, $v_L = 10^{-6}$ m^2/s and $\kappa_L = 10^{-7}$, we have $Re_L = 1.89 \times 10^5$ and $Ra_F = 3.56 \times 10^9$.

Two typical experiments were conducted as illustrated in Fig. 3. In the first experiment (Exp. 1, Fig. 3(a)–(c)), once the set-up was complete the investigators allowed 5 min to achieve a steady state condition. The positive buoyancy source was then turned on in the lower cavity and the investigators allowed another 5 min for the flow to become steady and stable. The negative buoyancy source was then turned on and was gradually increased in the upper cavity. The flow pattern gradually became stable. In the second experiment (Exp. 2, Fig. 3(d)–(f)), the process in Exp. 1 was reversed by first turning on the negative buoyancy source in the upper room. The flow visualization was achieved using the shadow graph principle.

2.3. Observations

During the first experiment, the heat source was switched on first, i.e., the fresh water source in the lower cavity. The supply flow rate was controlled by a control

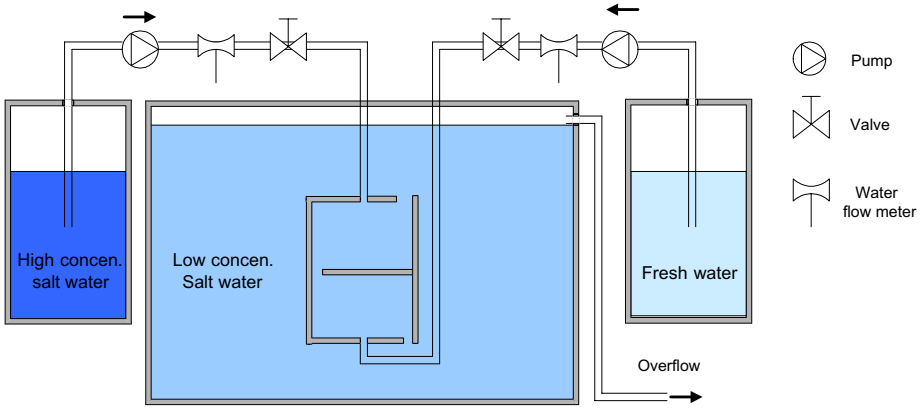

Fig. 2. A schematic diagram of the experimental set-up.

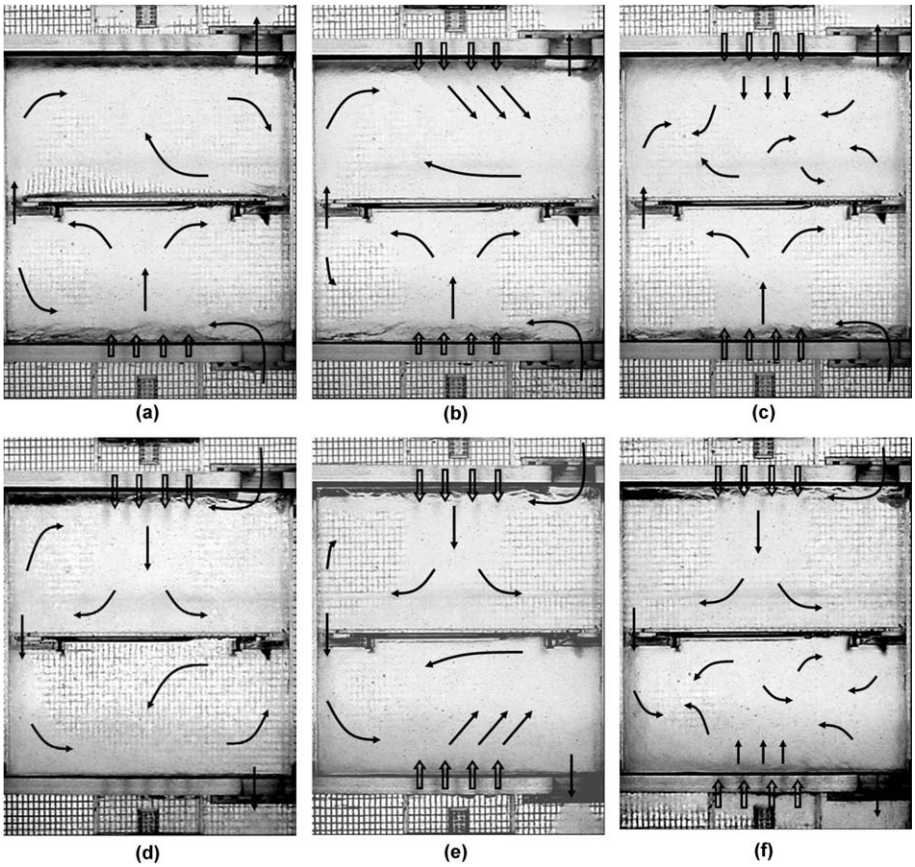

Fig. 3. Visualized flow patterns: (a) Exp. 1 – upward flow when the heat source acts alone in the lower cavity (heat source = 4 L/min, heat sink = 0 L/min); (b) Exp. 1 – upward flow when both heat source in the lower cavity and heat sink in the upper cavity act together (heat source = 4 L/min, heat sink = 2 L/min); (c) Exp. 2 – upward flow when both heat source in the lower cavity and heat sink in the upper cavity act together (heat source = 4 L/min, heat sink = 4 L/min); (d) Exp. 2 – downward flow when the heat source acts alone in the upper cavity (heat source = 0 L/min, heat sink = 4 L/min); (e) Exp. 2 – downward flow when both heat source in the lower cavity and heat sink in the upper cavity act together (heat source = 2 L/min, heat sink = 4 L/min); and (f) Exp. 2 – downward flow when both heat source in the lower cavity and heat sink in the upper cavity act together (heat source = 4 L/min, heat sink = 4 L/min).

valve to be 4 L/min. The positive buoyancy force led to an upward flow (Fig. 3(a)). A plume developed from the heat source, which drove the ambient water into the bottom cavity through its bottom opening. There was also an upward flow through the middle opening linking the two cavities. A stable stratification of flow in the lower cavity was established (Fig. 3(a)).

The cold source was then switched on in the upper cavity, and was also gradually increased to a flow rate of 4 L/min (Fig. 3(b)). The plume of the heat source in the lower cavity was upward and the plume of the cold source in the upper cavity was downward, but not as strong as the heat plume. The water flow direction was kept upward, first from the ambient to the bottom cavity, then through the middle opening into the upper cavity, flowing into the ambient through the upper opening. The stable stratification was still maintained in the lower cavity. Certain flow mixing in the upper cavity was also observed (Fig. 3(c)).

The second experiment (Exp. 2) reversed the procedure of Exp. 1, whereby the cold source was switched on first, i.e., the high concentration of salt water in the upper cavity. The supply flow rate was again controlled at 4 L/min. The negative buoyancy force set up a stable downward flow in the system with a stable stratification in the upper cavity (Fig. 3(d)).

The experiment was continued by switching on the heat source in the lower cavity, first at a flow rate of 2 L/min (Fig. 3(e)), and then at 4 L/min. Again, an upward plume in the lower cavity and a downward plume in the upper cavity were observed. However, the overall flow pattern was downward (see Fig. 3(f)).

The boundary conditions for the two final flow regimes (Fig. 3(c) and (f)) were identical. Although, both had two equal opposing buoyancy forces, two different overall flow patterns developed, i.e., one upward and one downward.

The same experiments were repeated more than 30 times by two different groups of investigators in early 2003 and late 2003, and the two differential flow patterns were always obtained, demonstrating that both solutions are physically very stable, which will be shown later by theoretical analysis. The experiments were also repeated with different source strengths, say 2 and 4 L/min. All these experiments showed the existence of two stable flow patterns under identical boundary conditions, but with two

different initial conditions. The mechanisms for the existence of the two stable flow patterns are explained by the following theoretical analyses.

3. Theoretical analysis

3.1. Macroscopic model

To provide physical insight into the mechanisms of the existence of two stable flow regimes in the two vertically connected open cavities, a simple macroscopic analysis was performed. The fluid temperature in each cavity was assumed to be uniform. This assumption may not be valid due to flow stratification; however, the resulting mathematical model was shown to provide sufficient physical insights into the bifurcation behaviour. The magnitude of the heat source in the lower cavity was E_1 (>0) and the magnitude of the heat sink in the upper cavity was E_2 (<0). It was also assumed that all other walls and the partition between the two cavities were adiabatic.

A heat balance equation for the fluid in each cavity can be written as follows:
For upward flows (Fig. 1(b)):

$$\begin{aligned} C_1M_1\frac{\mathrm{d}T_1}{\mathrm{d}t} &= E_1 + \rho C_p q(T_0 - T_1) \\ C_2M_2\frac{\mathrm{d}T_2}{\mathrm{d}t} &= E_2 + \rho C_p q(T_1 - T_2) \end{aligned} \tag{1}$$

For downward flows (Fig. 1(c)):

$$\begin{aligned} C_1M_1\frac{\mathrm{d}T_1}{\mathrm{d}t} &= E_1 + \rho C_p |q|(T_2 - T_1) \\ C_2M_2\frac{\mathrm{d}T_2}{\mathrm{d}t} &= E_2 + \rho C_p |q|(T_0 - T_2) \end{aligned} \tag{2}$$

Due to mass conservation, the volumetric flow rates through all three openings were equal as the fluid was assumed to be incompressible. The flow was driven by thermal buoyancy alone. It was further assumed that the flow through each opening was orifice-alike and thus a discharge coefficient C_D can be used to characterize the pressure-driven flow through each opening [18]. The volumetric flow rate q can be derived to be a function of the combined buoyancy force, the effective opening area and the discharge coefficients as

$$q|q| = [(C_DA)^*]^2\left(\frac{2gh_1(T_1 - T_0)}{T_0} + \frac{2gh_2(T_2 - T_1)}{T_0}\right) \tag{3}$$

The effective opening area $(C_DA)^*$ can be calculated from the areas of three openings:

$$(C_DA)^* = \frac{(C_{Dt}A_t)(C_{Dm}A_m)(C_{Db}A_b)}{\sqrt{(C_{Dt}A_tC_{Db}A_b)^2 + (C_{Dm}A_mC_{Db}A_b)^2 + (C_{Dm}A_mC_{Db}A_t)^2}} \tag{4}$$

We let $q > 0$ when the fluid flow is upward, and $q < 0$ when the fluid flow is downward. As seen from Eq. (3), if

$$\frac{2gh_1(T_1 - T_0)}{T_0} + \frac{2gh_2(T_2 - T_1)}{T_0} > 0$$

the flow rate is positive and the fluid flow is upward, and if

$$\frac{2gh_1(T_1 - T_0)}{T_0} + \frac{2gh_2(T_2 - T_1)}{T_0} < 0$$

the fluid flow is downward.

In order to study the qualitative dynamical behaviour of the system, i.e., the fixed points and their bifurcation, the following assumptions are made to simplify the governing equations. It is assumed that two cavities have identical geometrical parameters, as well as thermal storage capacity, i.e., $C_1M_1 = C_2M_2$; $h_1 = h_2$ defining that $\tau = \frac{t}{C_1M_1}$, $\theta_1 = T_1 - T_0$, $\theta_2 = T_2 - T_0$ and $b = \rho C_p(C_DA^*)\sqrt{\frac{2gh_1}{T_0}}$. Then the governing equations can be simplified as follows:
When $\theta_1 + \theta_2 > 0$:

$$\begin{aligned} \frac{\mathrm{d}\theta_1}{\mathrm{d}\tau} &= E_1 - b\theta_1\sqrt{\theta_1 + \theta_2} \\ \frac{\mathrm{d}\theta_2}{\mathrm{d}\tau} &= E_2 + b(\theta_1 - \theta_2)\sqrt{\theta_1 + \theta_2} \end{aligned} \tag{5}$$

When $\theta_1 + \theta_2 < 0$:

$$\begin{aligned} \frac{\mathrm{d}\theta_1}{\mathrm{d}\tau} &= E_1 + b(\theta_2 - \theta_1)\sqrt{-(\theta_1 + \theta_2)} \\ \frac{\mathrm{d}\theta_2}{\mathrm{d}\tau} &= E_2 - b\theta_2\sqrt{-(\theta_1 + \theta_2)} \end{aligned} \tag{6}$$

Thus, the dynamical behaviour of the flow in the two vertically connected open cavities may be described by Eqs. (5) and (6). The system of equations is non-linear, but reasonably simple. The fixed points can be obtained and the stability of these fixed points can be analyzed as a function of the control parameter E_2/E_1, i.e., the heat source ratio. Detailed derivation is provided in Appendix A. The effects of unequal geometrical parameters and unequal thermal storage capacities were also analyzed and studied. They are not included here for simplicity.

When the heat storage parameters and the stack heights in the two cavities are, respectively equal, the following conclusions from the simple non-linear analysis can be made. When $E_2/E_1 < -2$, the system has one stable fixed point, until when E_2/E_1 is greater than -2 and less than $-9/5$, another fixed point is generated from the infinity, which is unstable. When E_2/E_1 is greater than $-9/5$, a Hopf bifurcation occurs and the unstable fixed point turns into a stable one. The unstable periodic orbit enlarges as E_2/E_1 further increases. When E_2/E_1 is -1, the unstable periodic orbit becomes a line $\theta_1 + \theta_2 = 0$. When E_2/E_1 continues to increase, the unstable periodic orbit shrinks to another fixed point and disappears when $E_2/E_1 = -5/9$, which is another Hopf bifurcation point. After this bifurcation, the stable fixed point becomes an unstable one, which also disappears when $E_2/E_1 = -1/2$. For $E_2/E_1 > -1/2$, the system has only one stable fixed point. Thus, the system exhibits two stable fixed points when E_2/E_1 is between $-9/5$ and $-5/9$. Almost all experiments described in Section 2 were for $E_2/E_1 = -1$. It should be noted that we were not able to confirm the existence of Hopf bifurcation in our experiments.

3.2. An example

As an example, an open building with two vertically connected rooms was considered. This model building was inspired by the Manly Hydraulics Laboratory, which was completed in 1997 [19]. The building was built on a sloping site in Manly, Sydney, Australia. It was cooled in summer by a mixed-mode air-conditioning system, i.e., when the outdoor weather was suitable, natural ventilation was used. Air-conditioning is used during hot summer days. The floor and roof levels change by 1.2 m steps as the building progresses up the site. Plenums are located underneath the offices. For natural ventilation, outdoor air flows into these plenums via openings. The plenums communicate with offices above via vertical registers located in the 1.2 m steps, and via floor registers. Six solar chimneys are distributed fairly evenly over the roof, and serve to exhaust air from the offices.

For summer cooling, it is expected that high air temperatures in the solar chimneys will drive the airflows, while the cool storage in the plenums absorbs heat from the indoor air. The situation is the opposite at night. The solar chimneys are cooled by the outdoor air, while the plenums are heated by heat released from the thermal mass. At night, the heat absorbed during the day is released into the air. Effectively, there is a heat source in the lower room. The outdoors is cooler than the building and conduction and radiation heat loss in the building and the solar chimney effectively gives a heat sink in the upper rooms. Thus a situation of opposing buoyancy forces can result.

For simplicity, we assume a constant value of heat source of 1000 W in the lower room, i.e., $E_1 = 1000$ W. The heat sink strength in the upper room varies, thus we obtain different heat source ratios E_2/E_1. The dimension of each room is 4 m (long) × 3 m (wide) × 3 m (high) and there is an opening of 0.3 m^2 in the middle partition connecting the two rooms. The fluid is air. The two openings connecting the two rooms to the outdoors are also 0.3 m^2. The reference air density is 1.2 kg/m^3. The discharge coefficients for all openings are assumed to be 0.6. The fixed points are obtained as Eqs. (A4) and (A5), and Eqs. (A13) and (A14) in Appendix A. The bifurcation diagram is given in Fig. 4 for the airflow rates, and in Fig. 5 for the air temperatures in the two rooms as a function of the heat source ratio E_2/E_1.

At first, it is easier to examine the bifurcation diagram for ventilation flow rates in Fig. 4 than for air temperature in Fig. 5. The bifurcation diagram can be divided into five distinct zones in Fig. 4. In the zone between A_d and B_d (or B_u, here the subscript d stands for downward flows and the subscript u for upward flows), the heat source ratio $E_2/E_1 < -2$. There is only one stable fixed point for the flow rate shown in Fig. 4. The flow is downward. In this zone, the air temperature in the upper room (room 2) is less than that in the lower room (room 1), as shown in Fig. 5. This is simple to understand, as the downward flow is first cooled in the upper room (room 2), followed by heating in the lower room before the air is discharged through the bottom opening. The flow exhibits a kind of symmetry, as there is also one stable fixed point for the flow rate in Fig. 4 in the zone between E_u (or E_d) and F_u. The flow is upward in the zone between E_u (or E_d) and F_u. The air is first heated in the lower room. When $E_2/E_1 < 0$, i.e., there is a heat source in the lower room and a heat sink in the upper room, the air temperature in the upper room (room 2) is lower than that in the lower room (room 1). The air

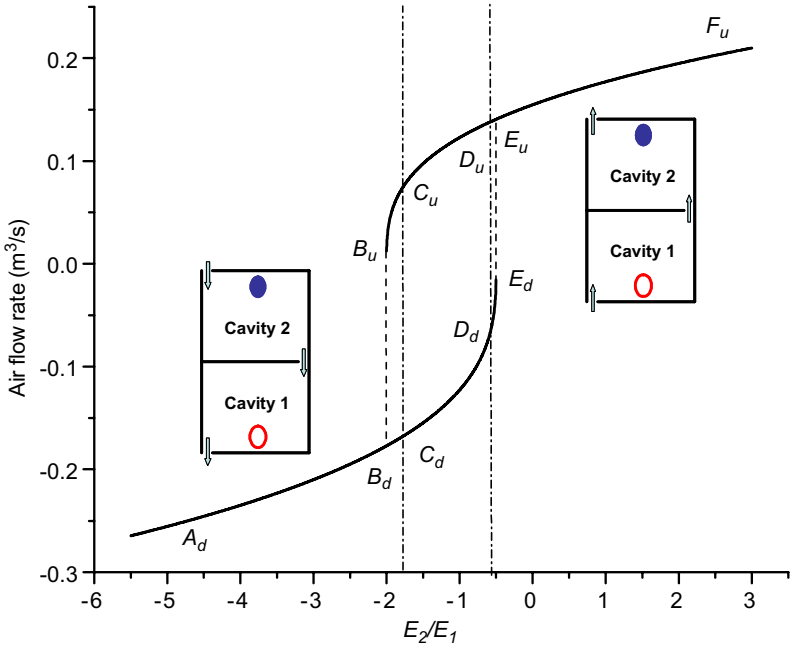

Fig. 4. Bifurcation diagram for ventilation flow rate as a function of heat source ratio E_2/E_1.

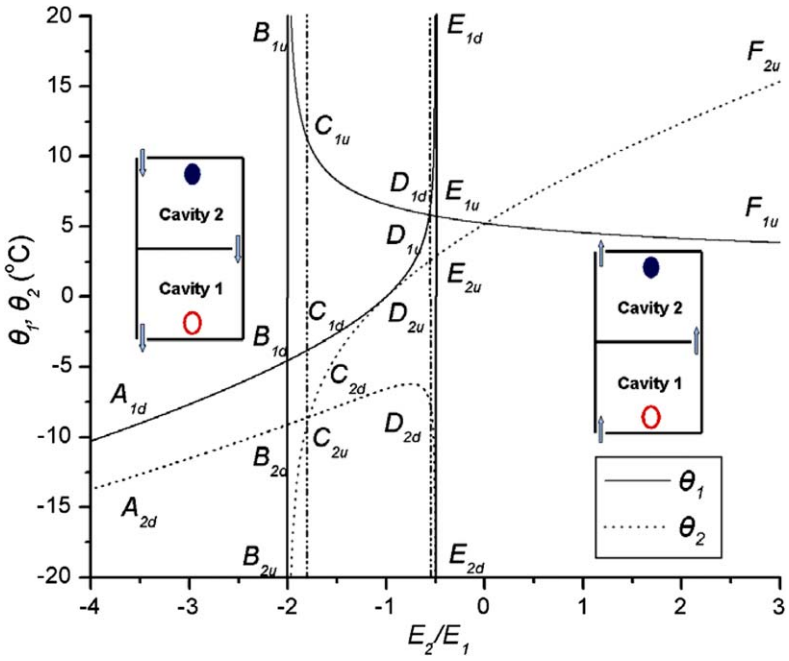

Fig. 5. Bifurcation diagram for the two room air temperatures as a function of the heat source ratio E_2/E_1. In the symbols, $X_{\#*}$, $X(A-F)$ indicates different points on the curves, the subscript #(1, 2) indicates the zone number, and $*$ (d,u) refers to downward and upward flows, respectively. The two vertical solid lines are the asymptotic lines as the temperatures approach the infinite values.

temperatures in the two rooms become equal when $E_2/E_1 = 0$, and as E_2/E_1 further increases, room 2 becomes warmer than room 1, due to the fact that the heat sink in the upper room turns into a heat source.

The flow in the middle zone between C_d (or C_u) and D_d (or D_u) has two stable fixed points. When the flow is upward (i.e., the flow rate in Fig. 4 is positive), the air temperature in room 1 is higher than that in room 2 (compare the line $C_{1u} - D_{1u}$ for the room 1 air temperature and the line $C_{2u} - D_{2u}$ for the room 2 air temperature in Fig. 5). When the flow is downward, the same trend can be observed (compare the line $C_{1d} - D_{1d}$ and the line $C_{2d} - D_{2d}$). It is also generally true that the overall air temperatures in the two rooms are higher when the flow is upward in this zone. Not shown in Fig. 4 is the existence of an unstable period orbit when $-1.8 < E_2/E_1 < -1$ or $-1 < E_2/E_1 < -5/9$.

What is interesting from this simple analysis is the existence of a Hopf bifurcation. In Fig. 4, it is shown that an unstable fixed point (upward flow) is generated from infinity at the point B_u. This is shown in Fig. 5 where the air temperatures in both rooms (B_{2u} and B_{1u}) are infinite. This upward flow is unstable. It can also be shown that the upward flow between B_u and C_u in Fig. 4 is unstable. As E_2/E_1 further increases from $-9/5$ to -1, the unstable fixed point (upward flow) turns into a stable one. Between the two stable fixed points, an unstable period orbit exists. With the same principle, an unstable fixed point (downward flow) is generated from infinity at the point E_d. The fixed point is also unstable between D_d and E_d. As E_2/E_1 further decreases from $-5/9$ to -1, the unstable fixed point (downward flow) turns into a stable one. Between the two stable fixed points, an unstable period orbit exists. When $E_2/E_1 = -1$, both unstable periodic orbits converge to a straight line $\theta_1 + \theta_2 = 0$.

This non-linear dynamical process can be further demonstrated by solving the governing equations (1) and (2) numerically using the fourth-order Runge–Kutta method. We present the phase portrait and vector field in Fig. 6 when $E_2/E_1 = -1$. Fig. 6 is obtained using different combinations of initial conditions of the two air temperatures. It is observed that different initial conditions converge to two different stable solutions of the air temperature, indicated by the two small circles in Fig. 6. Both the phase portrait and the vector field show the existence of a straight line (not shown) separating the two stable fixed points (circles). In Fig. 7, we present the phase portraits for six other different heat source ratios. When $E_2/E_1 = -2.5$ and $E_2/E_1 = 0.5$, all different initial conditions converge to one fixed point. When $E_2/E_1 = -1.85$ and $E_2/E_1 = -0.52$, we see a stable fixed point and an unstable fixed point. When $E_2/E_1 = -1.75$ and $E_2/E_1 = -0.56$, we see two stable fixed points and unstable periodic orbits may also be seen in both phase portraits, but located on two different sides of the straight line $\theta_1 + \theta_2 = 0$. This numerical result agrees well with the theoretical analysis shown in Figs. 4 and 5.

4. Analysis using computational fluid dynamics

4.1. Physical model and governing equations

The above theoretical analysis assumes that the fluid temperature in each cavity is uniform, which is not true, as shown by flow visualization experiment. Computational

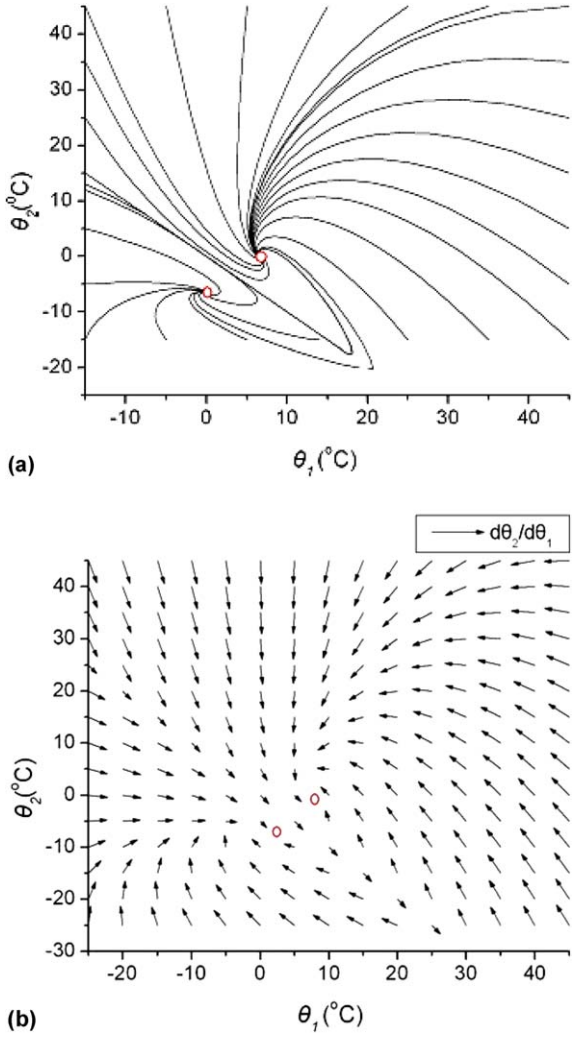

Fig. 6. Phase portrait and vector field when the heat source E_1 in the lower cavity (zone 1) and the heat sink E_2 in the upper cavity (zone 2) are equal in magnitude, i.e., $E_2/E_1 = -1$: (a) phase portrait; and (b) vector field. The two fixed points are indicated by two small circles.

fluid dynamics (CFD) simulations were carried out to confirm the bi-stable flow phenomenon. Our CFD simulations were carried out using a two-dimensional model. The model had the same physical parameters as in the example shown in Section 3.2. The dimensions of each cavity was 4 m (long) × 3 m (high), and there was an opening of 0.3 m^2 in the middle partition connecting the two cavities. The two openings linking the two cavities to the outdoor environment were also 0.3 m^2. The fluid was air. We chose an outdoor air temperature of 300 K. In the lower cavity, the heat source was a fixed constant at 1000 W. In the upper cavity, the heat source varied between −3000 W and 1000 W.

For simplicity here, CFD simulations were performed in two simple configurations. For Case 1, the heat source was distributed in both the upper ceiling and bottom floor of the two cavities. The middle opening was located in the middle of the middle partition. The two external openings were located in the vertical walls. For Case 2, the heat sources were modeled as two small volumes. The middle opening was located on the side of the middle partition. Both external openings were horizontal.

Two different types of boundary treatments were considered. In one simulation, the two-cavity model was located within a 40 m × 60 m large space which simulated the outdoor environment. In another simulation, pressure boundary conditions were applied at the two openings connecting to the ambient environment. The results shown here are for the latter boundary conditions.

The natural convection was considered to be two-dimensional, steady, and turbulent. All the thermo-physical parameters were assumed to be constant except for the density in the momentum equation following the Boussinesq approximation. The time-averaged governing equations based on the standard k–ε model are as follows:

Continuity:

$$\frac{\partial u}{\partial x}+\frac{\partial v}{\partial y}=0 \tag{7}$$

Momentum:

$$\frac{\partial uu}{\partial x}+\frac{\partial vu}{\partial y}=-\frac{1}{\rho}\frac{\partial p}{\partial x}+(v+v_t)\left(\frac{\partial^2 u}{\partial x^2}+\frac{\partial^2 u}{\partial y^2}\right) \tag{8}$$

$$\frac{\partial uv}{\partial x}+\frac{\partial vv}{\partial y}=-\frac{1}{\rho}\frac{\partial p}{\partial y}+(v+v_t)\left(\frac{\partial^2 v}{\partial x^2}+\frac{\partial^2 v}{\partial y^2}\right)+\beta g(T-T_0) \tag{9}$$

Energy:

$$\frac{\partial uT}{\partial x}+\frac{\partial vT}{\partial y}=\left(1+\frac{v}{\sigma_t}\right)\left(\frac{\partial^2 T}{\partial x^2}+\frac{\partial^2 T}{\partial y^2}\right) \tag{10}$$

Turbulent kinetic energy:

$$\frac{\partial uk}{\partial x}+\frac{\partial vk}{\partial y}=\left(v+\frac{v_t}{\sigma_k}\right)\left(\frac{\partial^2 k}{\partial x^2}+\frac{\partial^2 k}{\partial y^2}\right)+G_k-\varepsilon \tag{11}$$

Turbulent dissipation rate:

$$\frac{\partial u\varepsilon}{\partial x}+\frac{\partial v\varepsilon}{\partial y}=\left(v+\frac{v_t}{\sigma_\varepsilon}\right)\left(\frac{\partial^2 \varepsilon}{\partial x^2}+\frac{\partial^2 \varepsilon}{\partial y^2}\right)+\frac{\varepsilon}{k}(C_1G_k-C_2\varepsilon) \tag{12}$$

where the turbulent viscosity is defined as

$$v_t=C_\mu\frac{k^2}{\varepsilon} \tag{13}$$

and the turbulent energy production is defined as

$$G_k=v_t\left\{2\left[\left(\frac{\partial u}{\partial x}\right)^2+\left(\frac{\partial v}{\partial y}\right)^2\right]+\left(\frac{\partial u}{\partial y}+\frac{\partial v}{\partial x}\right)^2\right\} \tag{14}$$

The model coefficients in the standard k–ε model are $C_1 = 1.44$, $C_2 = 1.92$, $C_\mu = 0.09$, $\sigma_k = 1.0$, $\sigma_\varepsilon = 1.3$, $\sigma_t = 0.9$.

The computation was carried out using FLUENT 6.1, a commercial CFD code on a 2-D configuration. The

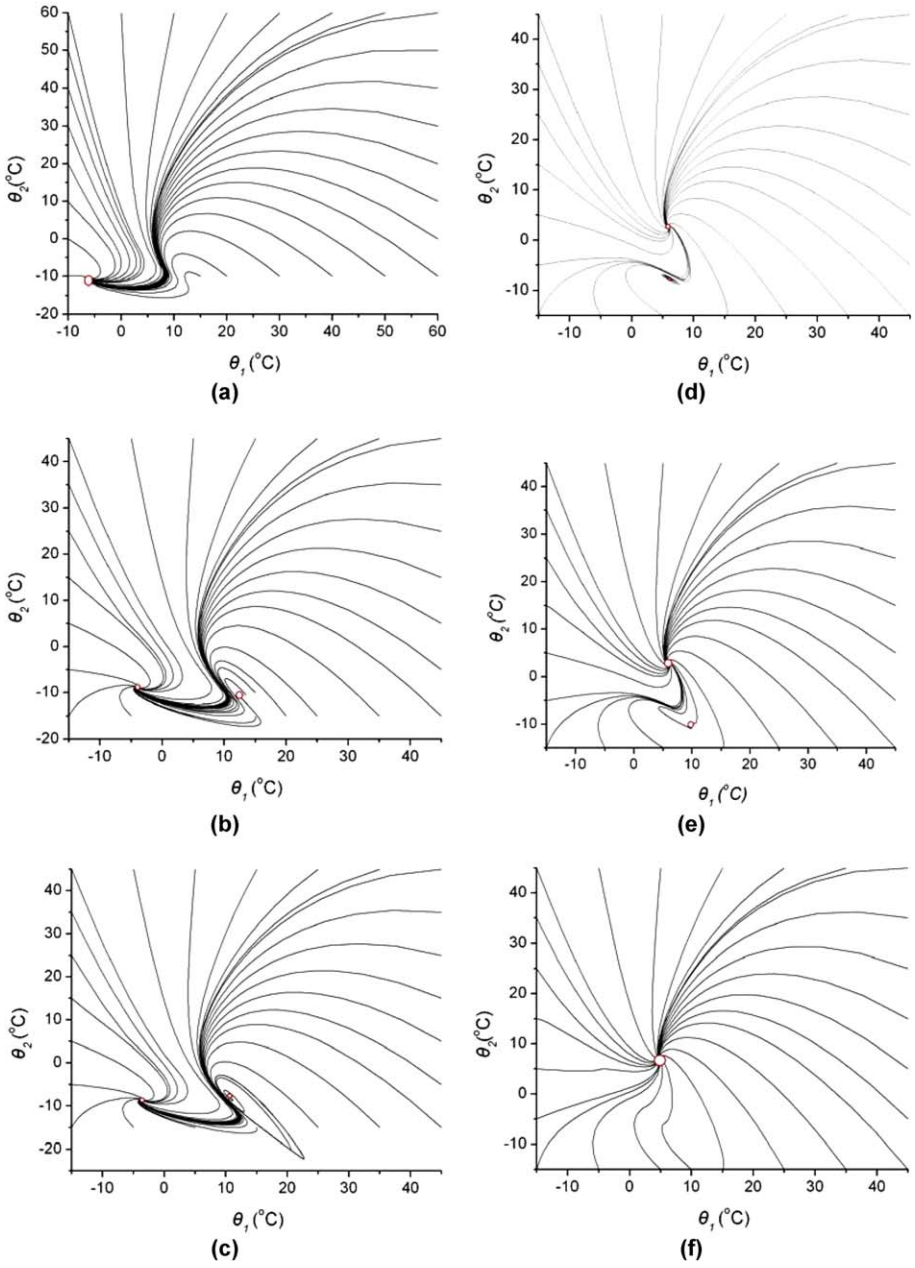

Fig. 7. Phase portraits for six different heat source ratios: (a) $E_2/E_1 = -2.5$; (b) $E_2/E_1 = -1.85$; (c) $E_2/E_1 = -1.75$; (d) $E_2/E_1 = -0.56$; (e) $E_2/E_1 = -0.52$; and (f) $E_2/E_1 = -0.5$.

SIMPLE algorithm for the pressure and velocity coupling was used. The QUICK scheme was used for the momentum equations, as well as the governing equations for the turbulence kinetic energy and the turbulence dissipation rate. The second-order upwind scheme was used for the energy equation.

Our solution tracking algorithm is based on that proposed by Albensoeder et al. [20]. In this approach, three main steps are implemented. Firstly, an original solution y_1 at the control parameter of λ_1 can be obtained using the conventional zero initial conditions. Secondly, for a step size $\Delta\lambda = \lambda_2 - \lambda_1$, a second solution y_2 at λ_2 can also be computed using the first solution y_1 at λ_1 as the initial condition. Finally, the third solution y_3 at λ_1 was recalculated backward using the second solution y_2 at λ_2 as the initial condition. Here we can get two solutions at λ_1. If the original and second solutions at λ_1 are identical, then we consider that there is no bifurcation and continue to compute the next solution for a step size of $\Delta\lambda$. Otherwise, a bifurcation point (i.e., turning point A) is assumed to exist, and then half of the step size will be tried to repeat the above steps. Iterations are carried out until location of the turning point is found with a sufficient accuracy. This solution tracking algorithm allows us to identify the stable fixed points, but not the unstable ones. Other more rigorous solution tracking algorithms can be found in [10,22].

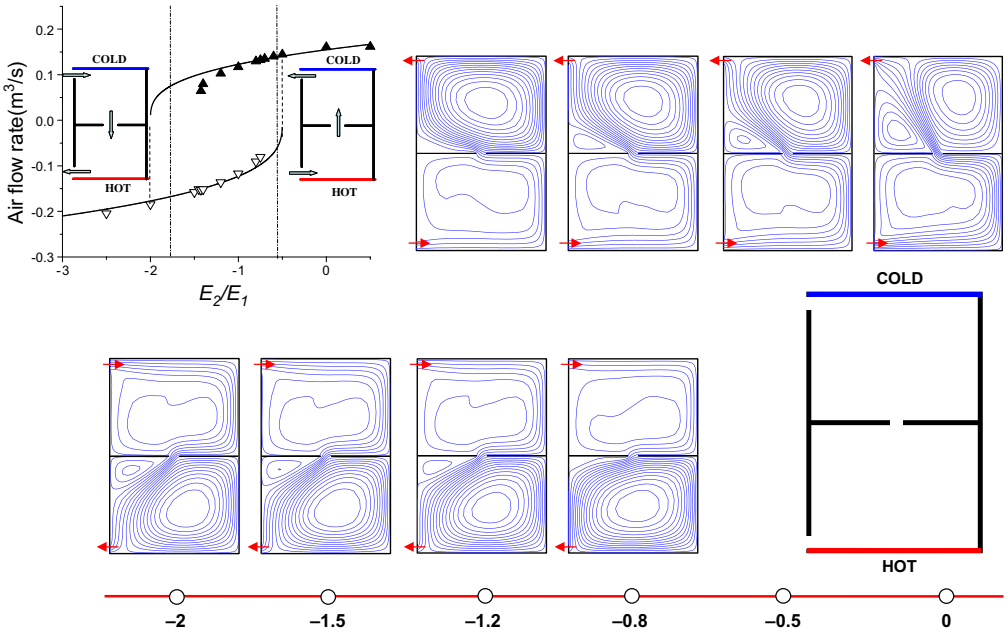

Fig. 8. The change of streamlines as a function of the heat source ratio E_2/E_1 (Case 1 – cold ceiling in the upper cavity and warm floor in the lower cavity, middle opening in the middle partition and two vertical external openings) (turning point: −1.475 to −0.700). The top left figure shows a comparison of predicted flow rate using CFD and the analytically obtained flow rate in Section 3.2.

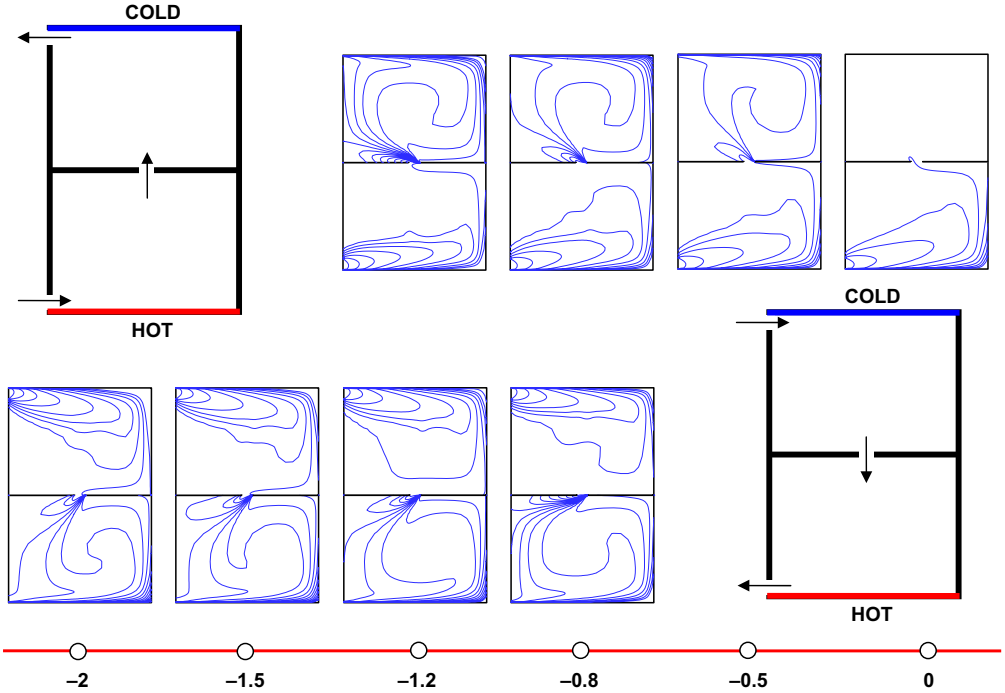

Fig. 9. Variations of isotherms as a function of the heat source ratio E_2/E_1 (Case 1 – cold ceiling in the upper cavity and warm floor in the lower cavity, middle opening in the middle partition and two vertical external openings) (turning point: −1.475 to −0.700).

4.2. Results and analysis

The streamlines and isotherms are plotted in Figs. 8 and 9 for Case 1, and in Figs. 10 and 11 for Case 2, respectively. Hysteresis phenomenon appeared in both cases. In Fig. 8, the streamlines were plotted at four representative heat ratios of −2, −1.5, −1.2 and −0.8 for the downward flows, and of −1.2, −0.8, −0.5 and 0 for the upward flows. It was found that two different flow patterns existed for the two heat ratios at −1.2 and −0.8. Examining the streamline plot at a heat ratio of −2, it was found that the incoming flow spread along the ceiling level, was cooled down by

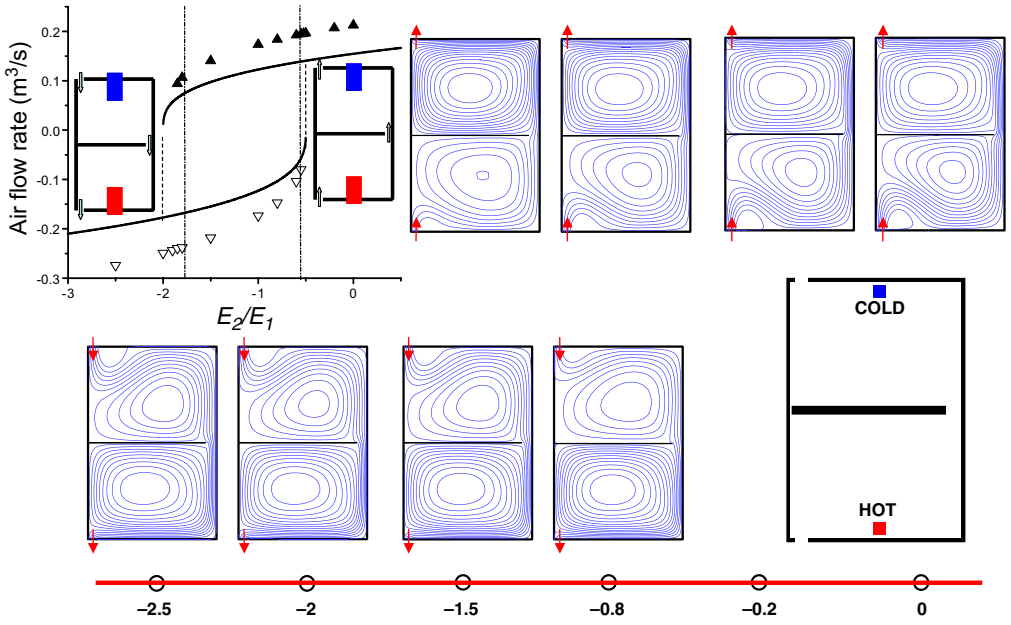

Fig. 10. Variations of streamlines as a function of the heat source ratio E_2/E_1 (Case 2 – volume heat sink in the upper cavity and volume heat source in the lower cavity, side opening in the middle partition and two horizontal external openings) (turning point: −1.900 to −0.525). The top left figure shows a comparison of predicted flow rate using CFD and the analytically obtained flow rate in Section 3.2.

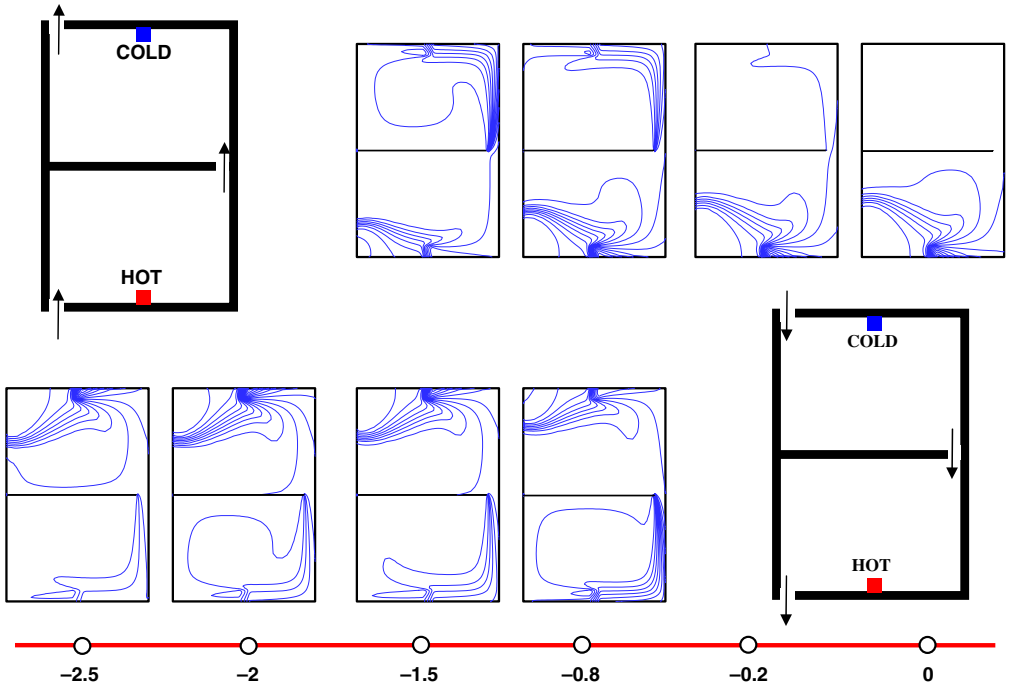

Fig. 11. Variations of isotherms as a function of the heat source ratio E_2/E_1 (Case 1 – volume heat sink in the upper cavity and volume heat source in the lower cavity, side opening in the middle partition and two horizontal external openings) (turning point: −1.900 to −0.525).

the cold ceiling (see Fig. 9), and fell along the right wall. A clockwise recirculation was formed in the upper cavity. The cold air fell through the middle opening and entering the lower cavity. The momentum of this flow, together with the positive buoyancy force (heating at the floor) created an anticlockwise recirculation in the lower cavity. There was a secondary recirculation formed at the top left corner of the lower cavity. This recirculation zone became smaller and smaller as the heat ratio further increased. The recirculation zone was almost non-existent at a heat ratio of −0.8. The flow patterns for the upward flows were nearly opposite to those for the downward flows. The flow in the lower cavity was anticlockwise in the lower cavity and clockwise in the upper cavity. There was also a secondary recircula-

tion zone in the upper cavity. The secondary recirculation was the greatest when the heat ratio was large (e.g., 0), gradually decreasing as the heat ratio reduced, and disappeared when the heat ratio was −1.2. The same flow pattern symmetry can also be found in the distribution of isotherms shown in Fig. 4.

No secondary recirculation existed when the two external openings were horizontal (Case 2), as shown in Fig. 10. The general flow recirculation in the two cavities followed a similar pattern as discussed for Case 1. The overall airflow rates through the open cavities are also shown in Figs. 2, 3, 9 and 10. Due to mass conservation, the airflow rates through all three openings were equal. When the flow was upward, the flow rate was positive, and when the flow was downward, the flow rate was negative. The flow rates predicted by CFD were surprisingly close to those predicted by the simple analytical solutions in Fig. 4. What was interesting was that the predicted ranges of heat ratios when the two solutions coexisted for the two cases were different. For Case 1, it was found that the turning point from the downward flow to upward flow was −0.700, and from upward flow to downward flow was −1.475. For Case 1, the turning point from downward flow to upward flow was −0.525, and from upward flow to downward flow it was −1.900. Our analytical solutions in Section 3.2 reveal that the range of heat ratios for the existence of two solutions was −1.8 and −5/9 (or −0.556). Assuming that the flow was fully mixed in both cavities was probably the main reason behind the differences between the CFD and analytical solutions. However, it is unknown why the bi-stable solution ranges were different between Case 1 and Case 2. One possible explanation is in the difference in flow patterns in the two situations considered here.

The heat ratio range of the bi-stable solutions was reasonably large. Assuming that the heat power in the lower cavity was 1000 W; the range of heat sinks in the upper cavity for the existence of two stable solutions was between −1475 W and −700 W for Case 1 – the smallest range among all the situations we examined. This means that the existence of the two stable solutions can be found at a wide range of heat ratios. The existence of the two stable solutions can be easily observed in a proper experimental set-up, as demonstrated in our experimental studies. Accurate devices for measuring salt water density were not available during the experiments. Salt water density was determined by the volume of water and the amount of salt added. Thus, there might be errors in our reported densities. The bi-stable flow patterns were repeated in more than 40 different experiments that were performed by two different groups of investigators.

5. Conclusions

A simple physical model was presented with two vertically connected open cavities, in which it is demonstrated, using visualization experiments, theoretical analysis and computational fluid dynamics simulations, that two stable solutions exist under a wide range of heat source ratios when flow is driven by opposing buoyancy forces. Two stable fixed points exist for a certain range of strength ratios of the heat source/sink. A hysteresis phenomenon was found between the stable steady flows. Hopf bifurcations also occur based on our theoretical analysis, assuming that the flow is fully mixed in each cavity. Both computational fluid dynamics simulations and the experimental visualization results verify this analysis, suggesting that the existence of two steady state solutions is not affected by the assumption of uniform temperature in the simple theoretical analysis.

As similar flows driven by opposing buoyancy forces exist in practical situations such as smoke spread in buildings, and natural ventilation of buildings, the findings in this paper can be practically very important. Li and Delsante [21] and Hunt and Linden [22] showed the existence of bi-stable flows in buildings ventilated by buoyancy and opposing wind. The fact that multiple stable equilibria exist in very simple buildings shows there is a need for further study of more realistic situations.

Acknowledgements

The work described in this paper was supported by two grants from the Research Grants Council of the Hong Kong Special Administrative Region, China (Project No. HKU 7020/02E and HKU 70019/01E).

Appendix A. Dynamical analysis

A.1. Fixed points and their stability for Eq. (5)

Denote the steady state solution (fixed point) of Eq. (5) as $(\theta_1^0,\ \theta_2^0)$, which satisfies the following equation:

$$E_1 = b\theta_1^0\sqrt{\theta_1^0+\theta_2^0}$$
$$E_2 = -b(\theta_1^0-\theta_2^0)\sqrt{\theta_1^0+\theta_2^0} \tag{A1}$$

It leads to:

$$\frac{E_1}{E_2} = \frac{b\theta_1^0\sqrt{(\theta_1^0+\theta_2^0)}}{-b(\theta_1^0-\theta_2^0)\sqrt{(\theta_1^0+\theta_2^0)}} = -\frac{\theta_1^0}{\theta_1^0-\theta_2^0} \tag{A2}$$

Eq. (A2) derives

$$\theta_2^0 = \left(1+\frac{E_2}{E_1}\right)\theta_1^0 \tag{A3}$$

Substituting Eq. (A3) into Eq. (A1) leads to:

$$(\theta_1^0)^3 = \frac{E_1^2}{b^2\left(2+\frac{E_2}{E_1}\right)} \tag{A4}$$

$$(\theta_2^0)^3 = \left(1+\frac{E_2}{E_1}\right)^3\frac{E_1^2}{b^2\left(2+\frac{E_2}{E_1}\right)} \tag{A5}$$

By the first equation of Eq. (A1) together with $E_1 > 0$, we conclude that $\theta_1^0 > 0$. Hence, to ensure that $\theta_1^0 + \theta_2^0 = \left(2 + \frac{E_1}{E_2}\right)\theta_1^0 > 0$, the condition $\frac{E_2}{E_1} > -2$ must be fulfilled. Thus, there is only one fixed point for Eq. (5) for $E_2/E_1 > -2$, and the fixed point is given by Eqs. (A4) and (A5).

To analyse the stability of the fixed point, the linearization equation of Eq. (5) at the fixed point $(\theta_1^0,\ \theta_2^0)$ must be considered, which is given as follows:

$$\begin{bmatrix} x' \\ y' \end{bmatrix} = \begin{bmatrix} -bw - \frac{b\theta_1^0}{2w} & \frac{-b\theta_1^0}{2w} \\ bw + \frac{b(\theta_1^0-\theta_2^0)}{2w} & -bw + \frac{b(\theta_1^0-\theta_2^0)}{2w} \end{bmatrix} \begin{bmatrix} x \\ y \end{bmatrix} \tag{A6}$$

where $\theta_1 = \theta_1^0 + x,\ \theta_2 = \theta_2^0 + x,\ w^2 = \theta_1^0 + \theta_2^0,\ x' = \mathrm{d}x/\mathrm{d}t,\ y' = \mathrm{d}y/\mathrm{d}t$.

The stability of the fixed point $(\theta_1^0,\ \theta_2^0)$ is governed by the eigenvalues of the matrix of the linearization Eq. (A6). If the real parts of two eigenvalues are negative, the fixed point is stable; if the real parts of two eigenvalues are positive, the fixed point is unstable, and if the real part of one eigenvalue is positive and another one is negative, the fixed point is a saddle. For Eq. (A6), two eigenvalues λ_1 and λ_2 satisfy

$$\lambda^2 + \beta\lambda + \gamma = 0 \tag{A7}$$

where

$$\beta = 2bw + \frac{b\theta_2^0}{2w}$$

$$\gamma = \frac{3}{2}b^2w^2$$

By Eq. (A7) two eigenvalues of Eq. (A5) are given as

$$\lambda_{1,2} = \frac{-\beta \pm \sqrt{\beta^2 - 4\gamma}}{2}$$

As

$$\beta = \frac{b\theta_1^0}{2w}\left(9 + 5\frac{E_2}{E_1}\right) \tag{A8}$$

$$\beta^2 - 4\gamma = \frac{b^2\theta_1^0}{4\left(2 + \frac{E_2}{E_1}\right)}\left(\left(\frac{E_2}{E_1}\right)^2 - 6\left(\frac{E_2}{E_1}\right) - 15\right) \tag{A9}$$

Hence, the real parts of two eigenvalues λ_1 and λ_2 are negative when $\frac{E_2}{E_1} > -\frac{9}{5}$ and positive when $-2 < \frac{E_2}{E_1} < -\frac{9}{5}$.

A.2. Fixed points and their stability for Eq. (6)

Denote the steady state solution (fixed point) of Eq. (6) as $(\theta_1^0,\ \theta_2^0)$, which satisfies the following equation:

$$\begin{aligned} E_1 &= -b(\theta_2^0 - \theta_1^0)\sqrt{-(\theta_1^0 + \theta_2^0)} \\ E_2 &= b\theta_2^0\sqrt{-(\theta_1^0 + \theta_2^0)} \end{aligned} \tag{A10}$$

This leads to

$$\frac{E_2}{E_1} = \frac{b\theta_2^0\sqrt{-(\theta_1^0 + \theta_2^0)}}{-b(\theta_2^0 - \theta_1^0)\sqrt{-(\theta_1^0 + \theta_2^0)}} = -\frac{\theta_2^0}{\theta_2^0 - \theta_1^0} \tag{A11}$$

Eq. (A11) derives

$$\theta_1^0 = \left(1 + \frac{E_1}{E_2}\right)\theta_2^0 \tag{A12}$$

Substituting Eq. (A12) into Eq. (A10) leads to

$$(\theta_2^0)^3 = -\frac{E_2^2}{b^2\left(2 + \frac{E_1}{E_2}\right)} \tag{A13}$$

$$(\theta_1^0)^3 = -\left(1 + \frac{E_1}{E_2}\right)^3\frac{E_2^2}{b^2\left(2 + \frac{E_1}{E_2}\right)} \tag{A14}$$

The second equation of Eq. (A10) shows that $\theta_2^0 > 0$ for $E_2 > 0$, while $\theta_2^0 < 0$ for $E_2 < 0$. Furthermore, $\theta_1^0 + \theta_2^0 = \left(2 + \frac{E_1}{E_2}\right)\theta_2^0 < 0$. Hence, Eq. (A10) has no root for $E_2 > 0$ and $E_1 > 0$; and has one root for $\frac{E_1}{E_2} > -2$. Thus, there is only one fixed point for Eq. (6) for $E_2/E_1 < -1/2$, and the fixed point is given by Eqs. (A14) and (A15).

To analyse the stability of the fixed point, the linearization equation of Eq. (6) at the fixed point $(\theta_1^0,\ \theta_2^0)$ must be considered, which is given as follows:

$$\begin{bmatrix} x' \\ y' \end{bmatrix} = \begin{bmatrix} -bw - \frac{b(\theta_2^0-\theta_1^0)}{2w} & bw - \frac{b(\theta_2^0-\theta_1^0)}{2w} \\ \frac{b\theta_2^0}{2w} & -bw + \frac{b\theta_2^0}{2w} \end{bmatrix} \begin{bmatrix} x \\ y \end{bmatrix} \tag{A15}$$

The two eigenvalues λ_1 and λ_2 of Eq. (A15) satisfy

$$\lambda^2 + \beta\lambda + \gamma = 0 \tag{A16}$$

where

$$\beta = 2bw - \frac{b\theta_1^0}{2w}$$

$$\gamma = \frac{3}{2}b^2w^2$$

$$w^2 = -(\theta_1^0 + \theta_2^0)$$

The two eigenvalues of Eq. (A15) are given as

$$\lambda_{1,2} = \frac{-\beta \pm \sqrt{\beta^2 - 4\gamma}}{2}$$

Furthermore, we have

$$\beta = -\frac{b\theta_2^0}{2w}\left(9 + 5\frac{E_1}{E_2}\right) \tag{A17}$$

$$\beta^2 - 4\gamma = -\frac{b^2\theta_2^0}{4\left(2 + \frac{E_1}{E_2}\right)}\left(\left(\frac{E_1}{E_2}\right)^2 - 6\left(\frac{E_1}{E_2}\right) - 15\right) \tag{A18}$$

Hence, the real parts of two eigenvalues λ_1 and λ_2 are negative when $\frac{E_1}{E_2} > -\frac{9}{5}$ and positive when $-2 < \frac{E_1}{E_2} < -\frac{9}{5}$.

A.3. Bifurcation

The above discussion shows that the real parts of the two eigenvalues for Eq. (5) are zero when $E_2/E_1 = -9/5$; while the real parts of the two eigenvalues for Eq. (6) are zero when $E_1/E_2 = -9/5$. Bifurcations would occur at this point. Here we will discuss the dynamical behaviour of Eq. (5) in detail as near the bifurcation point $E_2/E_1 = -9/5$. Since the real parts of the two eigenvalue λ_1 and λ_2 are negative for $\frac{E_1}{E_2} > -\frac{9}{5}$ and positive for $-2 < \frac{E_1}{E_2} < -\frac{9}{5}$, it is known that

$$\frac{\mathrm{d}}{\mathrm{d}(E_1/E_2)} Re(\lambda_{1,2}) < 0 \tag{A19}$$

Hence $E_1 + E_2 \approx -4/5E_1 < 0$.

First let $u = \sqrt{\theta_1 + \theta_2}$, then Eq. (5) can be written as

$$\frac{\mathrm{d}^2 u}{\mathrm{d}t^2} + \left(\frac{E_1 + E_2}{2u} + 2bu\right)\frac{\mathrm{d}u}{\mathrm{d}t} + \frac{b}{2}(bu^3 - (2E_1 + E_2)) = 0 \tag{A20}$$

Then Eq. (A20) can be written as

$$\begin{cases} \dfrac{\mathrm{d}u}{\mathrm{d}t} = \dfrac{E_1 + E_2}{2u} - bu^2 - v \\ \dfrac{\mathrm{d}v}{\mathrm{d}t} = \dfrac{b}{2}(bu^3 - (2E_1 + E_2)) \end{cases} \tag{A21}$$

The fixed point of Eq. (A21) is then given as

$$\begin{aligned} u_0 &= \left(\frac{2E_1 + E_2}{b}\right)^{1/3} \\ v_0 &= -\frac{3E_1 + E_2}{2u_0} \end{aligned} \tag{A22}$$

Denote

$$\begin{aligned} u &= u_0 + x \\ v &= v_0 + \sqrt{3/2}bu_0 y \end{aligned} \tag{A23}$$

Substituting (A23) into Eq. (A21), we obtain

$$\begin{cases} \dfrac{\mathrm{d}x}{\mathrm{d}t} = -\sqrt{\dfrac{3}{2}}bu_0 y - \left(\dfrac{E_1 + E_2}{2}\dfrac{x}{(u_0 + x)u_0} + 2bu_0 x + bx^2\right) \\ \dfrac{\mathrm{d}y}{\mathrm{d}t} = \sqrt{\dfrac{3}{2}}bu_0 x + \left(\dfrac{3}{2}b^2 u_0 x^2 + \dfrac{1}{2}b^2 x^3\right)/(\sqrt{3/2}bu_0) \end{cases} \tag{A24}$$

Let

$$\begin{aligned} f(x) &= -\left(\frac{E_1 + E_2}{2}\frac{x}{(u_0 + x)u_0} + 2bu_0 x + bx^2\right) \\ g(x) &= \left(\frac{3}{2}b^2 u_0 x^2 + \frac{1}{2}b^2 x^3\right)\Big/(\sqrt{3/2}bu_0) \end{aligned} \tag{A25}$$

Following the Poincaré–Andronov–Hopf bifurcation theorem [23], we evaluate the following coefficient,

$$\begin{aligned} a &= \frac{1}{16}(f_{xxx}(0)) + \frac{1}{16\sqrt{3/2}bu_0}(-f_{xx}(0)g_{xx}(0)) \\ &= -\frac{1}{16u_0^4}(3(E_1 + E_2) + 2(E_1 + E_2) - 4bu_0^3) \\ &= \frac{E_1}{16u_0^4}(3 - E_2/E_1) = \frac{E_1}{16u_0^4}\left(3 + \frac{5}{9}\right) > 0 \end{aligned} \tag{A26}$$

Thus by the Poincaré–Andronov–Hopf bifurcation theorem [23], a Hopf bifurcation occured when the ratio E_2/E_1 passes through the value $-9/5$ and an unstable periodic solution is generated for $E_2/E_1 > -9/5$.

Together with the conclusion of the stability of the fixed points for Eq. (5), we arrive at the following conclusions:

- Eq. (5) has a fixed point for $2 + E_1/E_2 > 0$.
- The fixed point is a source if $E_1/E_2 < -9/5$.
- The point $E_1/E_2 = -9/5$ is a Hopf bifurcation value. When the parameter E_1/E_2 is greater than $-9/5$, an unstable periodic orbit is generated.

References

[1] R.J.A. Janssen, R.A.W.M. Henkes, Influence of Prandtl number on instability mechanisms and transitions in a differentially heated square cavity, J. Fluid Mech. 290 (1995) 319–344.

[2] A. Javam, S.W. Armfield, Stability and transition of stratified natural convection flow in open cavities, J. Fluid Mech. 445 (2001) 285–303.

[3] J.P. Gollub, S.V. Benson, Many routes to turbulent convection, J. Fluid Mech. 100 (1980) 449–470.

[4] C.C. Jahnke, V. Subramanyan, D.T. Valentine, On the convection in an enclosed container with unstable side wall temperature distributions, Int. J. Heat Mass Transfer 41 (1998) 2307–2320.

[5] H. Stommel, Themohaline convection with two stable regimes of flow, Tellus 2 (1961) 230–244.

[6] O. Thual, J.C. McWilliams, The catastrophe structure of thermohaline convection in a two-dimensional fluid model and a comparison with low-order box models, Geophys. Astrophys. Fluid Dyn. 64 (1992) 67–95.

[7] J.A. Whitehead, Multiple T–S states for estuaries, shelves, and marginal seas, Estuaries 21 (1998) 281–293.

[8] J.A. Whitehead, W.G. Lawson, J. Salzig, Multistate flow devices for geophysical fluid dynamics and climate, Am. J. Phys. 69 (2001) 546–552.

[9] H.A. Dijkstra, M.J. Molemaker, Symmetry breaking and overturning oscillations in thermohaline-driven flows, J. Fluid Mech. 333 (1997) 169–198.

[10] H.A. Dijkstra, Non-linear Physical Oceanography: A Dynamical Systems Approach to the Large Scale Ocean Circulation and El Nino, Kluwer Academic Publishers., Dordrecht, 2000.

[11] J.B. Keller, Periodic oscillations in a model of thermal convection, J. Fluid Mech. 26 (3) (1966) 599–606.

[12] P. Welander, On the oscillatory instability of a differentially heated fluid loop, J. Fluid Mech. 29 (1) (1967) 17–30.

[13] R. Greif, Natural circulation loops, J. Heat Transfer 110 (1988) 1243–1258.

[14] Y.Y. Jiang, M. Shoji, M. Naruse, Boundary condition effects on the flow stability in a toroidal thermosyphon, Int. J. Heat Fluid Flow 23 (2002) 81–91.

[15] P.F. Linden, The fluid mechanics of natural ventilation, Ann. Rev. Fluid Mech. 31 (1999) 201–238.

[16] Y. Li, A. Delsante, Z.D. Chen, M. Sandberg, A. Andersen, M. Bjerre, P. Heiselberg, Some examples of solution multiplicity in natural ventilation, Build. Environ. 36 (2001) 851–858.

[17] C. Gladstone, A.W. Woods, On buoyancy-driven nature ventilation of a room with a heater floor, J. Fluid Mech. 441 (2001) 293–314.
[18] D. Etheridge, M. Sandberg, Building Ventilation Theory and Measurement, John Wiley & Sons, Chichester, 1996.
[19] Y. Li, A. Delsante, J. Symons, Upward flows in a multi-zone building with subfloor plenums and solar chimneys, in: Proceedings of Roomvent '98, Sweden, 14–17 June 1998.
[20] S. Albensoeder, H.C. Kuhlmann, H.J. Rath, Multiplicity of steady two-dimensional flows in two-sided lid-driven cavities, Theor. Computat. Fluid Dyn. 14 (2001) 223–241.
[21] Y. Li, A. Delsante, Natural ventilation induced by combined wind and thermal forces, Build. Environ. 36 (2001) 59–71.
[22] G.R. Hunt, P.F. Linden, Displacement and mixing ventilation driven by opposing wind and buoyancy, J. Fluid Mech. 527 (2005) 27–55.
[23] S. Wiggins, Introduction to Applied Nonlinear Dynamical Systems and Chaos, second ed., Springer-Verlag, New York, 2003.